Effect of ceramic coating thickness on fracture behaviour of coating structure under thermal shock cycles

L.H. Liang [a,*], X.H. Liu [b], L.F. Chen [a], Y.G. Wei [c]

[a] Beijing Key Lab of Health Monitoring and Self-Recovery for High-End Mechanical Equipment, College of Mechanical and Electrical Engineering, Beijing University of Chemical Technology, Beijing, 100029, China
[b] LNM, Institute of Mechanics, Chinese Academy of Sciences, Beijing, 100190, China
[c] College of Engineering, Peking University, Beijing, 100871, China

ARTICLE INFO

ABSTRACT

Ceramic coatings are commonly used to fulfil some form of protection function, such as thermal protection, electric isolation, or corrosion resistance. However, coating failure caused by mechanical mechanisms can reduce the effectiveness of these functions. In this study, the effect of the coating thickness of thermal barrier coatings on fracture behaviour was investigated to understand its importance and the related mechanical mechanisms. Thermal shock cycling experiments were conducted with a corresponding stress analysis based on the finite element method. The results indicate that coatings thicker than 300 μm are more likely to fail after a low number of cycles, the number of cycles at the failure of 500 μm coatings is only 16.6% of that of 100 μm coatings, and the underlying mechanism can be explained as the larger compressive stress influence of thicker coatings. The residual compressive stress increased to 125 MPa only after ten cycles for 300 μm coatings.

1. Introduction

Ceramic coatings parts used in turbine engine often experience high temperatures and thermal shock environments during normal service, and the gradually accumulated thermal stress induces the spallation of surface ceramic coatings [1–15]. Thick ceramic coatings deposited on alloy substrates can protect the internal alloy substrate more effectively; however, the interface between thick coatings and the substrates cracks easily, in addition to the high cost of such coatings [16–22]. Ye et al. found that the number of thermal fatigue cycles before failure for 200 μm-thick coatings were higher than for 500 μm-thick coatings [23]. Saeedi et al. found that thermal shock resistance properties of functionally graded material coatings with five layers are better than those of coatings with a bilayer at 1100 °C in the thermal shock experiment. In particular, a better interface bond strength improved the thermal shock resistance properties [24]. Li et al. investigated the effect of thickness of coatings on the fracture mode under the three-point bending test. They found that interface cracking dominated for thicker coatings, and multiple transverse cracking dominated for thinner coatings. The different failure modes were explained based on different control stresses [25]. Liu et al. also reported the effect of thickness of coatings under four-point bending despite the same control stress [26]. Zhu et al. found

similar effect of thickness of coatings under tension [27].

In addition to the thickness of the coatings in the macroscopic view, the microstructure and composition in the microscopic view influences the fracture properties. Thermal shock heating experiments using a laser heating method were performed to check the crack propagation at the interface. Surface coating expansion occurred owing to the high temperature at the surface. This was confined by the substrates, which induced compressive stress in the coatings and tensile stress in the substrates, leading to interface cracking [28]. The thermal shock properties are related to the microstructure and composition of the coatings. Rangaraj and Kokini found that the fracture toughness was sensitive to the composition of graded coatings in a thermal shock experiment performed using laser heating [29,30]. Ghasemi et al. found that the microstructure of thermal barrier coatings changed as columnar crystals, similar to those prepared by the electronic beam physical vapour deposition method after laser remelting. The surface strain tolerance increased, thus enhancing the thermal shock resistance properties [31]. Wang et al. found that the thermal shock resistance properties of nanostructured coatings were better than those of conventional coatings with microstructures on the micron scale [30]. Liang et al. reported similar results and found different microscopic fracture paths in nanostructured coatings (fractures along grain boundaries) and conventional

---

Table 1
Material properties of the substrate (Sub), bond coat (BC), and topcoat (TC) [2, 39,40].

Material properties	Sub: GH3128	BC: NiCoCrAlY	TC: 8YSZ
E (GPa)	200	186	18
μ	0.3	0.3	0.2
ρ (kg/m^3)	7800	7320	5200
α ($\times 10^{-6}$/K)	18.7	15.1	10.2
σ_Y (MPa)	627	270	—
c (J/(kg K))	437	501	450
k (W/(m K))	21	4.3	1.53

coatings (grain fractures) [32].

Research has found that thermal shock failure can occur when the coatings experience thermal shock quenching. The ceramic coatings are in a tensile stress state because of the temperature drop on the surface and the confinement effect on their contracting trend from the substrates. This stress induces coating cracking, and after multiple thermal shock cycles, the cracks can propagate to and along the interface with the substrate resulting in the spallation of coatings [2,33–40]. The failure is attributed to mismatches of mechanical parameters, such as the elastic modulus, thermal expansion coefficient, and Poisson's ratio, between the ceramic coatings and the alloy substrates, which induce mismatch stress and thermal stress. In fact, the stress distribution is complicated owing to the temperature gradient along the coating thickness direction.

The optimisation design of coatings depends on a deep understanding of the mechanical properties, thermal protection properties, and underlying stress mechanism. In this study, the effect of thickness of coating on fracture under thermal shock cycles was systematically investigated by combining thermal shock experiments with corresponding finite element analysis. The coating spallation area was checked first by applying thermal shock cycling for coating samples with different thicknesses. The detailed cracking in coatings and interfaces was further observed by scanning electron microscopy (SEM) after different numbers of thermal shock cycles. The effects of the coating thickness on the fracture area and number of cycles to failure were analysed. The corresponding finite element model was developed, and the thermal stress distribution and evolution of coatings with different thicknesses were compared to determine the underlying mechanism.

2. Experimental method

8YSZ (8 wt% Y_2O_3-stabilised ZrO_2) coating samples with coatings sprayed on a Ni-based superalloy substrate (GH3128) were prepared with a substrate thickness of 2.75 mm. This included a pre-sprayed alloy bond coat of approximately 50 μm using commercial NiCoCrAlY powder. Coatings with thicknesses of 100, 300, and 500 μm were prepared to check the coating thickness effect. The spraying process was carried out using an atmospheric plasma spraying system (A-200, Sulzer-Metco F4 gun, Pfäffikon, Switzerland). The coating samples were fabricated at the Shanghai Institute of Ceramics, Chinese Academy of Sciences, Shanghai,
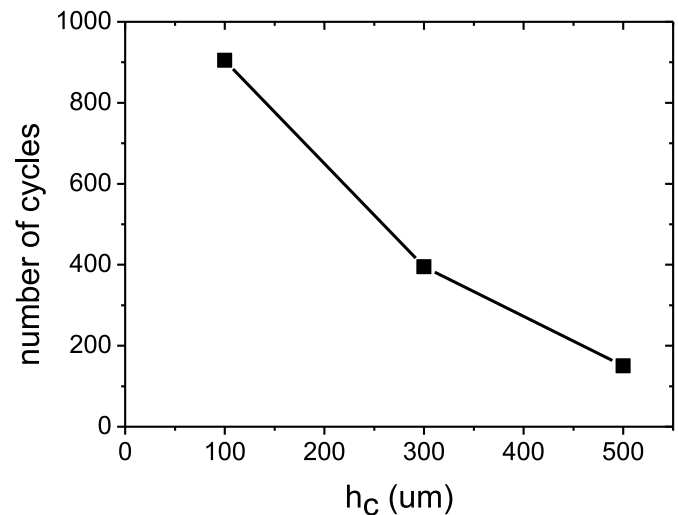

Fig. 2. The number of thermal shock cycles of coating spallation decreases with increasing coating thickness.

China. The detailed preparation process and parameters are listed in Table 1 in Ref. [41].

The samples were placed in a heated muffle furnace at 1000 °C for 5 min, and then, they were rapidly immersed in water at a temperature of 10 °C. This is described as one-time thermal shock cycling. Note that when the temperature is higher than 1000 °C, the thermal growth oxides grows fast and phase transformation occurs, the thickness effect will interact with other effects, so only 1000 °C was selected here to study pure coating thickness effect. At the same time, the coating surface and sample cross-section were observed after every five cycles, and the crack initiation, extension, and coating fracture were examined using a scanning electron microscope (SU1510). When 50% of the coatings had peeled off, the coating was defined as having failed.

3. Experimental results

Fig. 1 compares the surface morphology of coating spallation for three different coating thickness samples after thermal shock cycles. The figure shows that for the 100 μm coating, only local spallation occurred even after 905 cycles. However, block spallation occurred at lower cycles for the 300 and 500 μm coatings. For the 500 μm coatings, severe spallation appeared after only 150 cycles. It is clear that the number of cycles to coating failure decreases with increasing coating thickness, the number of cycles at failure of 500 μm coatings is only 16.6% of that of 100 μm coatings as shown in Fig. 2.

To understand the crack origin, the evolution of the cross-sectional microscopic morphology of the coating samples after thermal shock cycling is shown for the three different coating thicknesses in Fig. 3 and Figs. 5 and 6, respectively. Fig. 3 shows that the thermal growth oxide

Fig. 1. Surface morphology of coating spallation for coating thicknesses of 100, 300, and 500 μm from top to bottom, respectively, after 905, 395 and 150 thermal shock cycles.
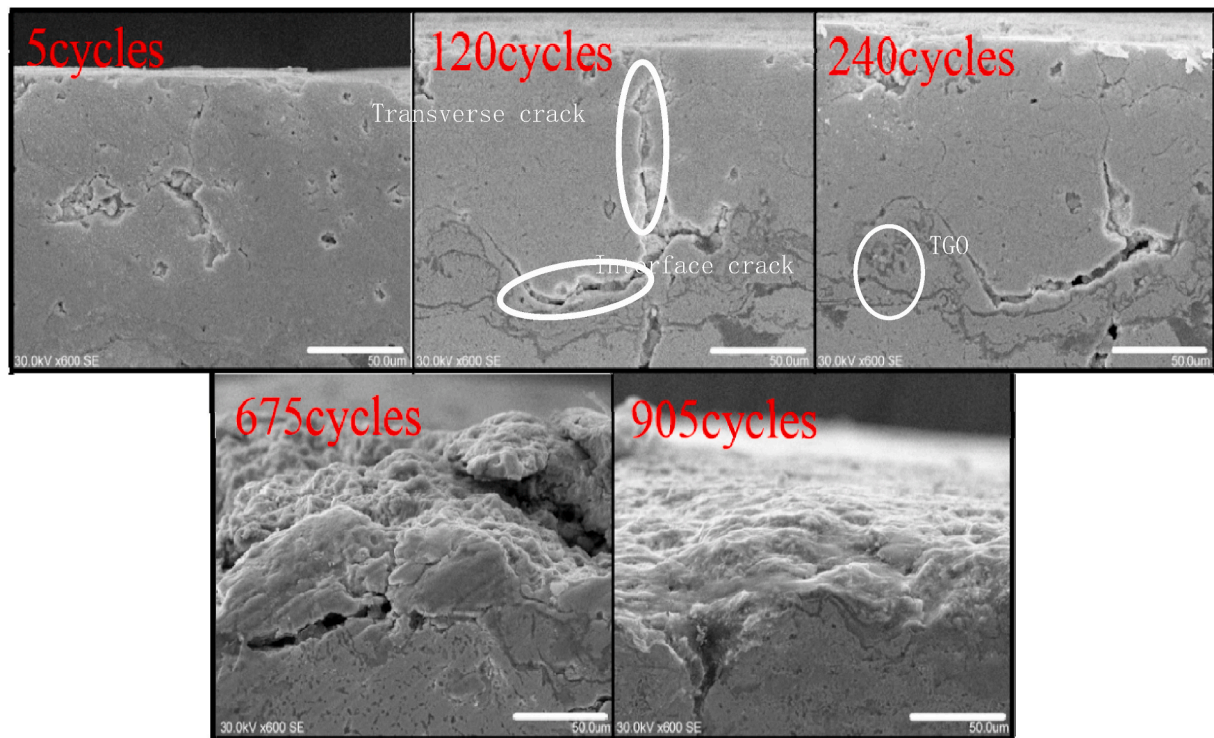
Fig. 3. Cross-section of 100 μm-coating sample obtained by SEM after different numbers of thermal shock cycles with the scale bar of 50 μm.
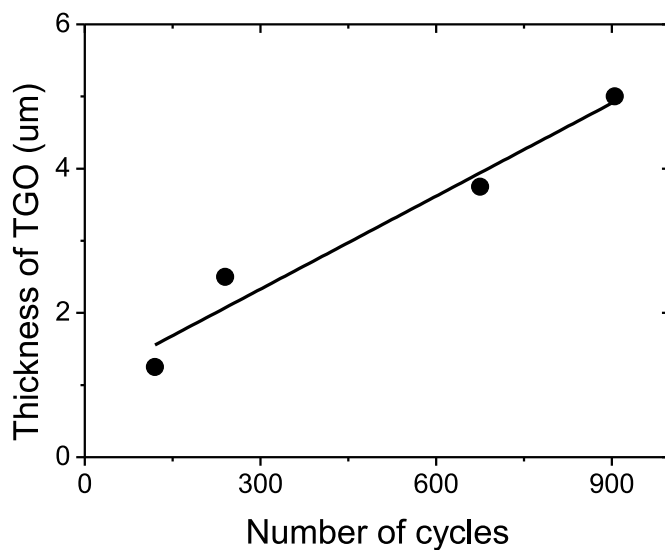

Fig. 4. Thickness of TGO increases with thermal cycles for 100 μm coating sample.

(TGO) of 1.3 μm formed in the 100 μm coating, and the interface crack occurred near the TGO in addition to the transverse cracks after 120 cycles. The local spallation of the coating occurred at the boundary after 675 cycles, and the thickness of TGO reaches 3.8 μm. The spallation area increased obviously after 905 cycles. Although TGO grows linearly after multiple thermal cycles as shown in Fig. 4 for 100 μm coating samples, the thickness of TGO is smaller than 6 μm, this thin TGO has a positive effect on the resistance against thermal shock as discussed in Ref. [42]. Note that the thickness effect of TGO has been studied, the induced stress increases with increasing thickness of TGO [43,44], especially when the thickness of TGO is larger than 8 μm [43]. Considering TGO is thin here and its effect is not obvious, which will be neglected in the next finite

element model.

Fig. 5 shows the process from transverse cracking (Fig. 5(a)) to interface cracking of the 300 μm coating, which started after 80 cycles (Fig. 5(c)). The interface crack was clearly observed at the TGO/coating interface after 190 cycles (Fig. 5(d)). The interface crack propagated further after 240 cycles (Fig. 5(e)). The cracks extended through the interface, and the coating spallation occurred at the boundary after 310 cycles (Fig. 5(f)). Fig. 6 shows that the interface crack appeared after 80 cycles for the 500 μm coating (Fig. 6(e)). The cracks extended, and the interface fractured after 120 cycles (Fig. 6(f)). The results indicate that the coating spallation mainly originated from the interface fracture, and the interface crack was often initiated at the boundary (two ends, as shown in Fig. 1) with the stress concentration. To analyse the stress effect, the finite element method was used to calculate the thermal stress evolution and distribution described in the next section.

4. Finite element model of thermal shock

To understand the experimental phenomena and the related mechanical mechanism, the thermal stress during the thermal cycles was analysed by developing a two-dimensional finite element model equivalent to the experimental samples. Fig. 7 shows a finite element model of the thermal barrier coating structure, including three layers: top coating (TC), bond coat (BC), and substrate (Sub). Note that TGO was not considered here since it is thin and the effect is not obvious. Abaqus FEA was used to simulate the transient stress in the structure during the heating-up and cooling-down cycles. The transient stress was caused by the thermal mismatch induced by the different thermal expansion coefficients of different layers. The Sub and BC were considered as ideal elastic-plastic materials, the TC was considered as an elastic material, and isotropic materials were assumed. The coupled temperature effect was considered using the CPE4T 2D plane strain element. The related material parameters, such as the elastic modulus E, Poisson's ratio μ, yield stress σ_Y, density ρ, thermal expansion coefficient α, specific heat c, and thermal conductivity k are listed in Table 1. Five models with TC thicknesses of 100, 200, 300, 400 and 500 μm were established to check
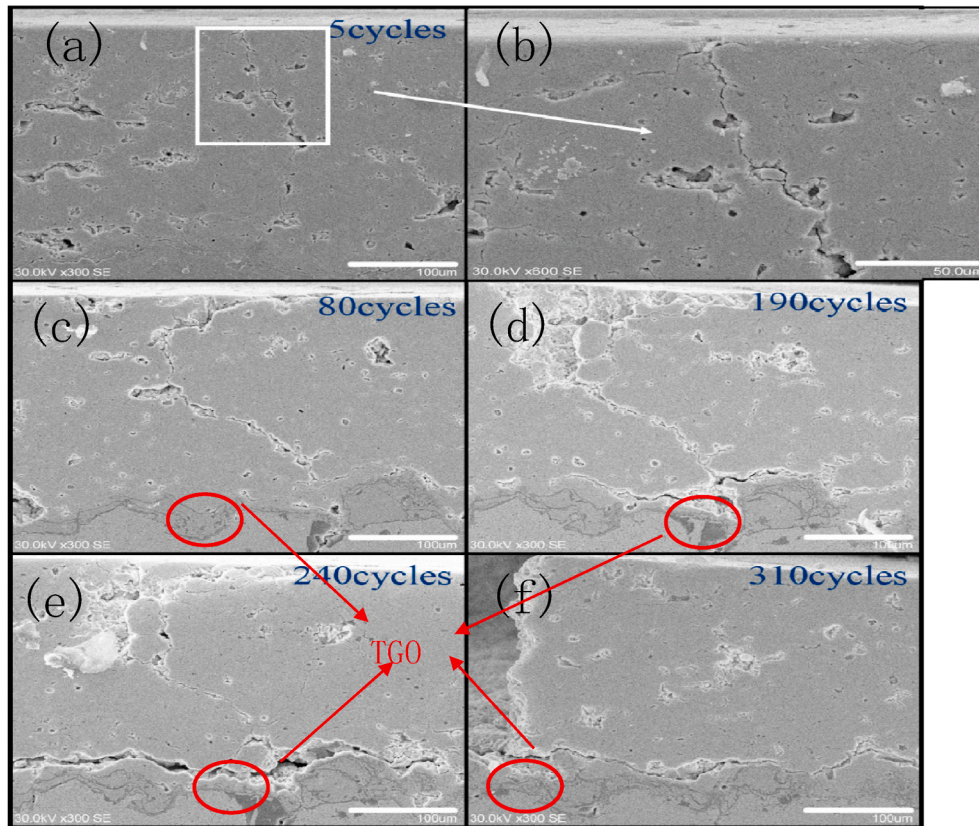
Fig. 5. Cross-section of 300 µm-coating sample obtained by SEM after different numbers of thermal shock cycles with scale bar of 100 µm except for enlargement in (b).

the coating thickness effect. Two analysis steps of temperature-displacement coupling were established. In the first heating-up step, the model was heated by surface heat radiation. The ambient temperature was set to 1000 °C. The structure temperature was increased from 10 °C to 1000 °C in 5 min similar to the experimental conditions. In the second cooling down step, the natural convection of water was applied on all surfaces of the coating structure, and the heat transfer coefficient was considered as 1000 Wm^{-1}K^{-1}. The temperature of the water is set to 10 °C. A process of heating and cooling is regarded as a thermal shock cycle, and the cycling was performed several times.

The simulation is based on the differential equation of thermal conduction:

$$\frac{\partial T}{\partial t} = \frac{k}{c\rho}\left(\frac{\partial^2 T}{\partial x^2} + \frac{\partial^2 T}{\partial y^2}\right) \tag{1}$$

where T is the temperature, t is time, x-direction is parallel to the substrate surface, and y-direction is along the substrate thickness, referring to point A in Fig. 5 as the origin point. The third type of boundary condition is applied:

$$q = h(T - T_f) \tag{2}$$

where q is the density of the heat flux, T_f represents the environmental temperature of thermal convection, and h is the heat transfer coefficient. According to Fourier's law $k\frac{\partial T}{\partial x} = q$,

$$k\frac{\partial T}{\partial x} = h(T - T_f) \tag{3}$$

can be obtained. According to the differential equation of force equilibrium,

$$\frac{\partial \tau_{xy}}{\partial y} + \frac{\partial \sigma_x}{\partial x} = 0$$

$$\frac{\partial \tau_{xy}}{\partial x} + \frac{\partial \sigma_y}{\partial y} = 0 \tag{4}$$
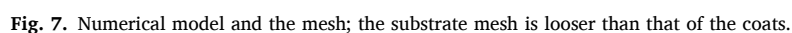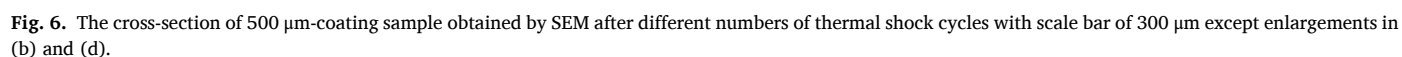
geometry equation,

$$\varepsilon_x = \frac{\partial u}{\partial x}, \varepsilon_y = \frac{\partial v}{\partial y}, \gamma_{xy} = \frac{\partial v}{\partial x} + \frac{\partial u}{\partial y} \tag{5}$$

and physical equation,

$$\sigma_x = \frac{E}{1-\mu^2}(\varepsilon_x + \mu\varepsilon_y) - \frac{E\alpha T}{1-\mu}$$

$$\sigma_y = \frac{E}{1-\mu^2}(\varepsilon_y + \mu\varepsilon_x) - \frac{E\alpha T}{1-\mu} \tag{6}$$

$$\tau_{xy} = \frac{E}{2(1+\mu)}\gamma_{xy}$$

the analysis solution is difficult for this thermal force coupling problem, and a numerical solution was obtained based on the finite element method.

In Fig. 7, the detailed boundary conditions are as follows: point A: displacement in the x- and y-directions $u = v = 0$, point B: displacement in the y-direction $v = 0$, and rigid body displacement of the structure was restrained. The initial temperature was 10 °C, and heating and cooling were performed by applying the temperature and convection boundary conditions vertically to every surface, as mentioned above.

Fig. 6. The cross-section of 500 μm-coating sample obtained by SEM after different numbers of thermal shock cycles with scale bar of 300 μm except enlargements in (b) and (d).

Fig. 7. Numerical model and the mesh; the substrate mesh is looser than that of the coats.

5. Simulation results of stress distribution and evolution

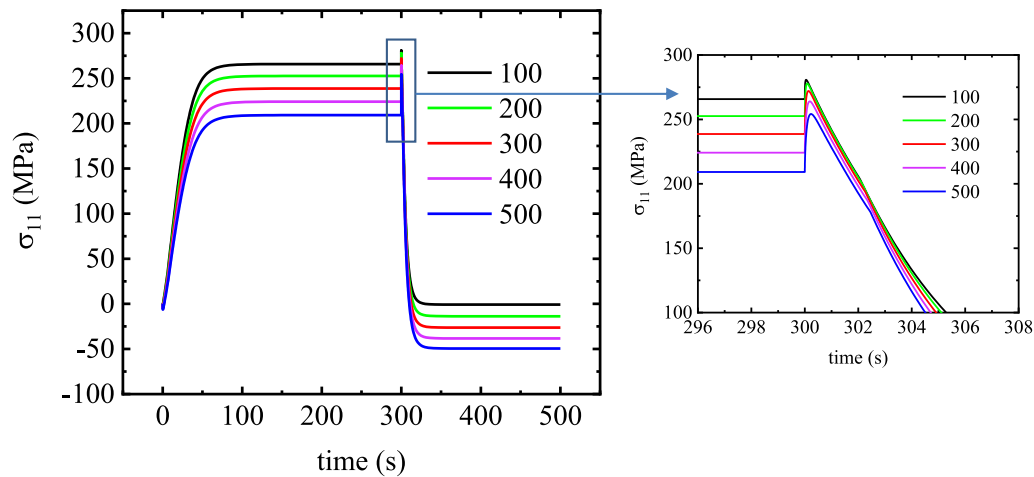Considering that the coating surface stress is homogeneous except at the two ends, the stress at the middle point C of the coating surface, as shown in Fig. 8, was analysed first. The normal stress σ_{11} evolution of point C with time is shown in Fig. 8, where the first 300 s correspond to the initial heating step and the next 150 s correspond to the cooling down (quenching) step. It is clear that the tensile stress increases

Fig. 8. Normal stress σ_{11} evolution of point C on coating surface for different coating thicknesses (100, 200, 300, 400 and 500 μm).
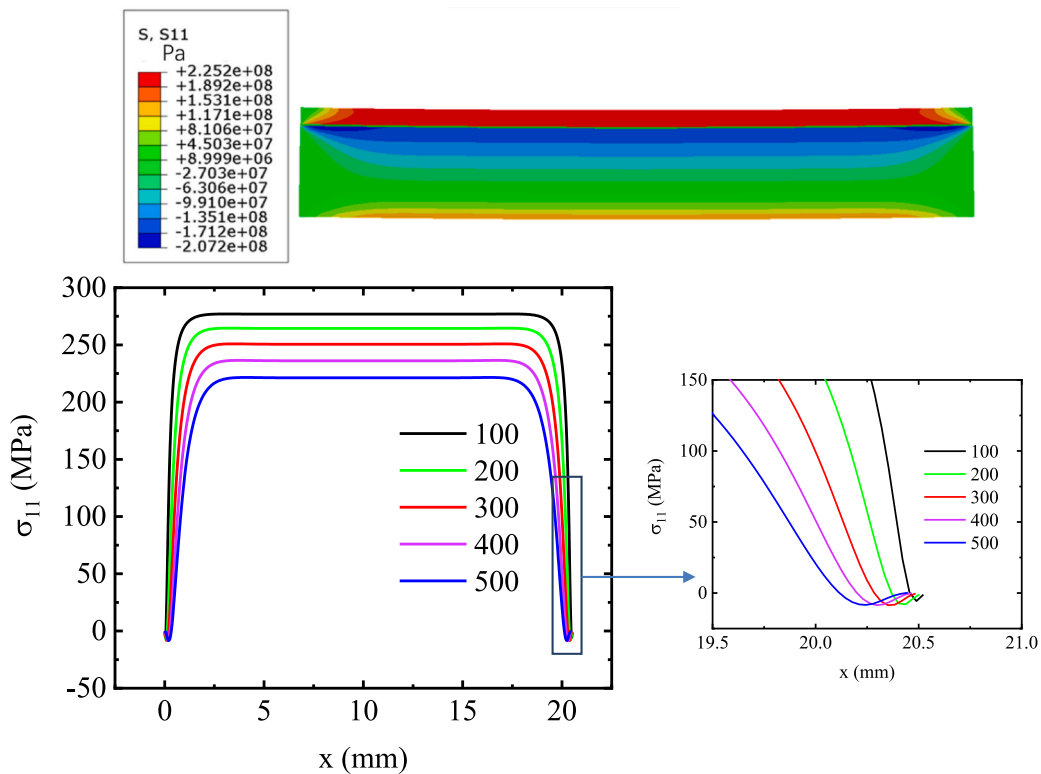

Fig. 9. (a) Normal stress σ_{11} distribution in cross-section of the model with coating thickness of 500 μm, 0.01 s after start of quenching. (b) Normal stress σ_{11} distribution along surface of coatings with different thicknesses (100, 200, 300, 400 and 500 μm).

initially during the heating process and then remains stable up to the initial cooling period. The coating surface is in a tensile stress state in the heating step owing to a thermal mismatch between the coating and the substrate and the smaller thermal expansion coefficient of the coatings. The stable tensile stress (approximately 260 MPa for the 100 μm coating) decreases with increasing thickness of the coatings, which is attributed to the smaller tensile effect from the substrates. The substrates were in a compressive stress state, and the substrate compressive stress increased with increasing thickness of the coatings (Supplementary Fig. 1). During quenching, the normal stress of the coating decreased rapidly after a slight enhancement (see enlarged graph of the zone in Fig. 8) and became compressive, which increased with increasing

thickness of the coatings, owing to the higher temperature gradient in the thicker coatings (Supplementary Fig. 2). The instance of a slight enhancement of tensile stress (20–40 MPa) at the beginning of cooling is attributed to the instant shrinkage of the surface coating. The tensile stress induced transverse cracking in the surface coatings, which was clear and in agreement with the previous analysis [45], especially for the thinner coatings with the higher tensile stress. However, the compressive stress during cooling induced interface cracking between the coatings and the substrates, which is especially evident for thicker coatings with a higher compressive stress of 50 MPa. These results agree with the experimental results [16] and the results of coatings under three-point bending that coating surface cracking dominates in thin coatings and
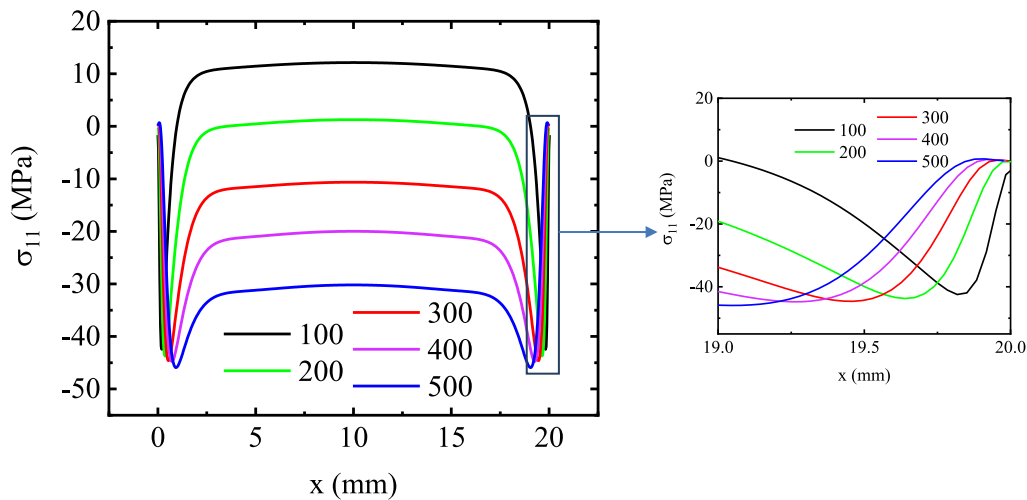
Fig. 10. Normal stress σ_{11} distribution along surface of coatings with different thicknesses, 15 s after start of quenching.
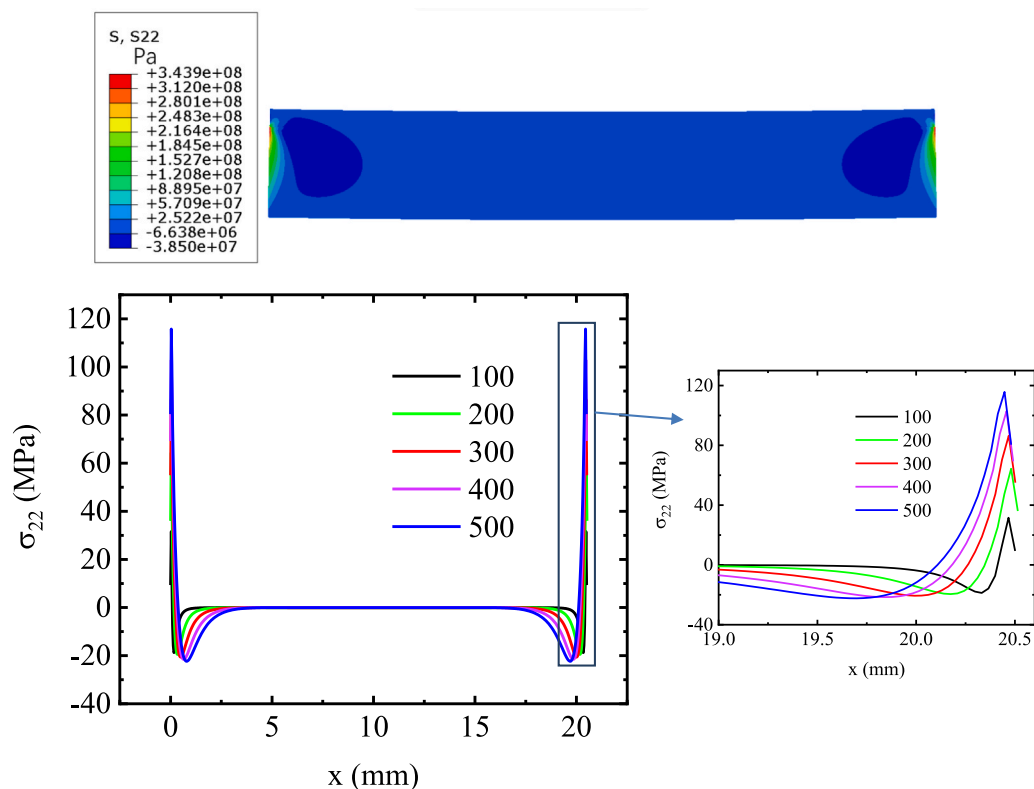

Fig. 11. (a) Normal stress σ_{22} distribution in cross-section of the model with coating thickness of 500 μm, 0.01 s after start of quenching. (b) Normal stress σ_{22} distribution along TC/BC interface for different coating thicknesses (100, 200, 300, 400 and 500 μm).

the interface cracking dominates in thick coatings [25].

The normal stress σ_{11} distribution of the coating surface in the x-direction 0.01 s after the start of quenching is shown in Fig. 9. The tensile stress is homogeneous along the surface except at the ends (the confinement effect on the boundary of the substrate is almost neglected and the stress is about zero), and the tensile stress is lower for the thicker coatings (Fig. 9(b)) due to the smaller confinement effect of the substrate, similar to the stress distribution during heating. Fig. 10 shows that the normal stress of the coating surface transformed into a compressive stress 15 s after the start of quenching for the 200 μm, 300 μm, 400 μm and 500 μm coatings, and the stress changed significantly at

the two ends. At this time, the compressive stress in the bond coat reached 120 MPa for the 300 μm coating structure (Supplementary Fig. 3), and the substrates were in a tensile stress state (Supplementary Fig. 4). Fig. 11 shows the distribution of the normal stress σ_{22} in the y-direction at the interface between the coating and substrate. It is clear that the normal stress σ_{22} is almost zero except near the ends, where the stress goes through a rapid change from a tensile to a compressive state along the interface from the end to nearby (Fig. 11(b)), attributed to the large temperature gradient at the boundary during quenching transient as showed in Supplementary Fig. 5, and the stress change zone near the ends is larger for thicker coatings. The results indicate that interface

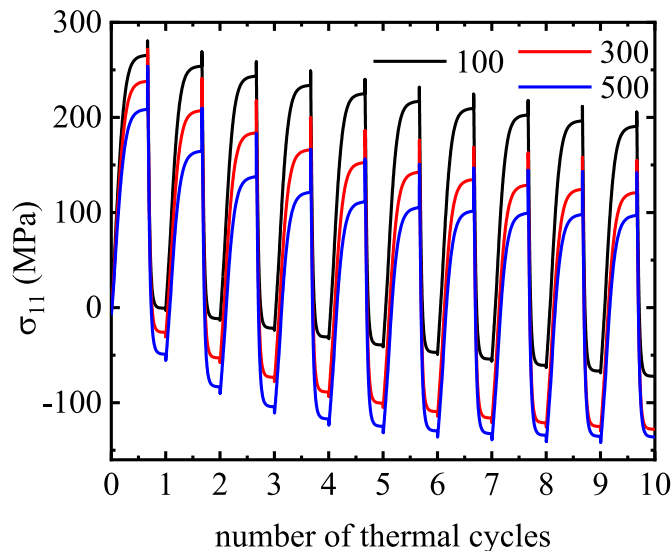**Fig. 12.** Displacement U₂ distribution in the model with 300 μm coating after ten thermal shock cycles.

Fig. 13. Normal stress σ_{11} evolution of point C on coating (100, 300 and 500 μm) surface during ten thermal shock cycles.

cracking initiates from the ends, in agreement with the experimental results (Fig. 1).

Furthermore, thermal shock cycling for the 300 μm-coating structure was simulated. Fig. 12 shows the displacement u_2 distribution in the y-direction after ten cycles. It is clear that the displacements were more significant at the two ends and the coating was warped up, which is related to the residual strain in the plastic substrates. As this residual strain increased with thermal shock cycling, coating spallation finally occurred. Fig. 13 shows the normal stress σ_{11} evolution at point C of the coating surface with the number of thermal cycles. It is clear that the change trends of the stress are the same in every cycle, but the maximum tensile stress decreased and the maximum compressive stress increased with increasing numbers of cycles. The residual compressive stress increased from 26 MPa after one cycle to 125 MPa after ten cycles for 300 μm coatings (to 72 MPa for 100 μm and 136 MPa for 500 μm). The compressive stress increased slightly with further continuous cycles. However, there is no obvious change in the normal stress σ_{22} in the y-direction at the interface after several thermal shock cycles, as shown in Fig. 14, implying the normal stress σ_{11} in the x-direction is dominant for thickness effect and the larger compressive stress induced serious interface cracking of the thicker coatings. Because the plastic deformation is irreversible, with the accumulation and increase of the residual stress, the stress at the interface reaches the strength and coating spallation occurs.

6. Conclusion

The effect of the thickness of coatings on spallation and the related stress mechanism under thermal shock cycles were investigated by conducting thermal shock experiments and finite element analysis. The experiments revealed that the number of thermal cycles needed to initiate coating spallation is smaller for thicker coatings, e.g., the coatings of 500 μm spalled only after 150 cycles, and the interface cracking was more significant for thicker coatings. The finite element simulation results indicate that the coating surface during one thermal cycle first moves into a tensile stress state during heating, and later moves into a
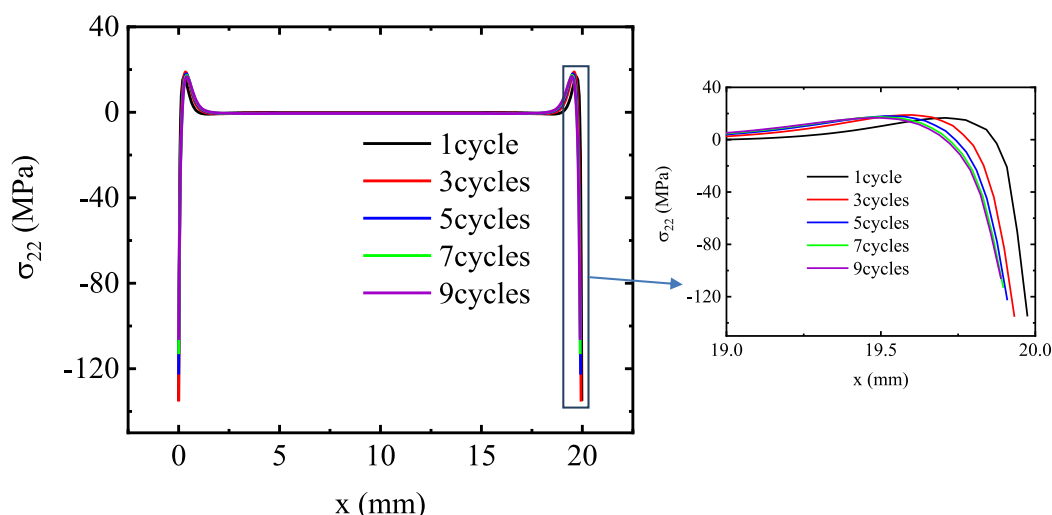

Fig. 14. Normal stress σ_{22} distribution along TC/BC interface for the model with 300 μm coating after different numbers of thermal shock cycles.

compressive stress state during quenching. The tensile stress decreases and the compressive stress increases with increasing numbers of cycles, the residual compressive stress increased to 136 MPa only after ten cycles for 500 μm coatings, being about two times of 72 MPa for 100 μm coatings. The compressive stress is higher for the thicker coatings, and the zones of change of stress at two ends is also larger. This explains the effect of the thickness of coatings on the failure and is a valuable input for design purposes.

Declaration of competing interest

The authors declare that they have no known competing financial interests or personal relationships that could have appeared to influence the work reported in this paper.

Acknowledgements

Appendix A. Supplementary data

Supplementary data related to this article can be found at https://doi.org/10.1016/j.ceramint.2021.12.368.

References

[1] N.P. Padture, M. Gell, E.H. Jordan, Thermal barrier coatings for gas-turbine engine applications, Science 296 (2002) 280–284.
[2] L. Wang, Y. Wang, X.G. Sun, J.Q. He, Z.Y. Pan, C.H. Wang, Thermal shock behavior of 8YSZ and double-ceramic-layer La2Zr2O7/8YSZ thermal barrier coatings fabricated by atmospheric plasma spraying, Ceram. Int. 38 (2012) 3595–3606.
[3] H.Y. Zhang, Z.W. Liu, X.B. Yang, H.M. Xie, Interface failure behavior of YSZ thermal barrier coatings during thermal shock, J. Alloys Compd. 779 (2018) 686–697.
[4] X.M. Sun, L.Z. Du, H. Lan, H.F. Zhang, R.Y. Liu, Z.G. Wang, S.G. Fang, C.B. Huang, Z.A. Liu, W.G. Zhang, Study on thermal shock behavior of YSZ abradable sealing coating prepared by mixed solution precursor plasma spraying, Surf. Coating. Technol. 397 (2020), 126045.
[5] Y.P. Cao, X.J. Ning, Q.S. Wang, Thermal shock behavior of Ba(Mg1/3Ta2/3)O3-YSZ double-ceramic-layer thermal barrier coatings prepared by atmospheric plasma spraying, Surf. Coating. Technol. 409 (2021), 126842.
[6] X.Y. Guo, Z. Lu, H.Y. Park, L. Li, J. Knapp, Y.G. Jung, J. Zhang, Thermal properties of La2Zr2O7 double-layer thermal barrier coatings, Adv. Appl. Ceram. 118 (2018) 1–7.
[7] H.I. Seo, D. Kim, K.S. Lee, Crack healing in mullite-based EBC during thermal shock cycle, Coatings 9 (2019) 585.
[8] R.J. Wang, W.Q. Duan, K.D. Wang, X. Dong, Z.J. Fan, X.S. Mei, W.J. Wang, S. Zhang, Computational and experimental study on hole evolution and delamination in laser drilling of thermal barrier coated nickel superalloy, Opt Laser. Eng. 107 (2018) 161–175.
[9] A.G. Koushali, M. Sameezadeh, M. Vaseghi, P. Safarpour, Analytical and numerical investigations of the crack behavior in thermal barrier coatings under the trip thermal load, Surf. Coating. Technol. 337 (2018) 90–96.
[10] K. Bobzin, L.D. Zhao, W. Wietheger, T. Königstein, Key influencing factors for the thermal shock resistance of La2Zr2O7-based multilayer TBCs, Surf. Coating. Technol. 396 (2020), 125951.
[11] L. Zhe, S.W. Myoung, H.S. Kim, M.S. Kim, J.H. Lee, Y.G. Jung, J.C. Jang, U. Paik, Microstructure evolution and interface stability of thermal barrier coatings with vertical type cracks in cyclic thermal exposure, J. Therm. Spray Technol. 22 (2013) 671–679.
[12] Z.Y. Pan, Y. Wang, C.H. Wang, X.G. Sun, L. Wang, The effect of SiC particles on thermal shock behavior of Al2O3/8YSZ coatings fabricated by atmospheric plasma spraying, Surf. Coating. Technol. 206 (2012) 2484–2498.
[13] Z. Lu, S.W. Myoung, Y.G. Jung, G. Balakrishnan, J. Lee, U. Paik, Thermal fatigue behavior of air-plasma sprayed thermal barrier coating with bond coat species in cyclic thermal exposure, Materials 6 (2013) 3387–3403.
[14] J.F. Zhang, X.H. Zhong, Y.L. Cheng, Y. Wang, Z.H. Xu, X.L. Chen, H.M. Ma, Y. Zhao, X.Q. Cao, Thermal-shock resistance of LnMgAl11O19 (Ln = La, Nd, Sm, Gd) with magnetoplumbite structure, J. Alloys Compd. 482 (2009) 376–381.
[15] Y.Q. Xiao, L. Yang, W. Zhu, Y.C. Zhou, Z.P. Pi, Y.G. Wei, Delamination mechanism of thermal barrier coatings induced by thermal cycling and growth stresses, Eng. Fail. Anal. 121 (2021), 105202.
[16] F.Z. Lu, W.Z. Huang, H.T. Liu, Mechanical properties and thermal shock resistence of 8YSZ-Al2O3 composite coatings with different thicknesses, J. Therm. Spray Technol. 28 (2019) 1893–1905.
[17] K. Torkashvand, E. Poursaeidi, M. Mohammadi, Effect of TGO thickness on the thermal barrier coatings life under thermal shock and thermal cycle loading, Ceram. Int. 44 (2018) 9283–9293.
[18] D. Chicot, G. Marot, P. Araujo, N. Horny, A. Tricoteaux, M.H. Staia, J. Lesage, Effect of some thermal treatments on interface adhesion toughness of various thick thermal spray coatings, Surf. Eng. 22 (2006) 390–398.
[19] H.P. Xiong, A. Kawasaki, Y.S. Kang, R. Watanabe, Experimental study on heat insulation performance of functionally graded metal/ceramic coatings and their fracture behavior at high surface temperatures, Surf. Coating. Technol. 194 (2005) 203–214.
[20] A. Ashofteh, M. Mosavi Mashhadi, A. Amadeh, S. Seifollahpour, Effect of layer thickness on thermal shock behavior in double-layer micro- and nano-structured ceramic top coat APS TBCs[J], Ceram. Int. 43 (2017) 13547–13559.
[21] A. Ashofteh, M. Mosavi Mashhadi, A. Amadeh, Thermal shock behavior of multilayer and functionally graded micro- and nano-structured topcoat APS TBCs, Ceram. Int. 44 (2017) 1951–1963.
[22] C.T. Yu, H. Liu, J. Zhang, A. Ullah, Z.B. Bao, C.Y. Jiang, S.L. Zhu, F.H. Wang, Gradient thermal cycling behavior of a thermal barrier coating system constituted by NiCoCrAlY bond coat and pure metastable tetragonal nano-4YSZ top coat, Ceram. Int. 45 (2019) 15281–15289.
[23] M.H. Li, X.F. Sun, W.Y. Hu, H.R. Guan, Thermal shock behavior of EB-PVD thermal barrier coatings, Surf. Coating. Technol. 201 (2007) 7387–7391.
[24] B. Sacedi, A. Sabour, A.M. Khoddami, Study of microstructure and thermal shock behavior of two types of thermal barrier coatings, Mater. Corros. 60 (2009) 695–703.
[25] Li X.N. Li, L.H. Liang, J.J. Xie, L. Chen, Y.G. Wei, Thickness-dependent fracture characteristics of ceramic coatings bonded on the alloy substrates, Surf. Coating. Technol. 285 (2014) 1039–1047.
[26] H.Y. Liu, L.H. Liang, Y.B. Wang, Y.G. Wei, Fracture characteristics and damage evolution of coating systems under four-point bending, Int. J. Appl. Ceram. Technol. 13 (2016) 1043–1052.
[27] W. Zhu, L. Yang, J.W. Guo, Y.C. Zhou, C. Lu, Numerical study on interaction of surface cracking and interfacial delamination in thermal barrier coatings under tension, Appl. Surf. Sci. 315 (2014) 292–298.
[28] C.W. Wu, C.G. Huang, G.N. Chen, Interface delamination of the thermal barrier coating subjected to local heating, Sci. China Technol. Sci. 53 (2010) 3168–3174.
[29] S. Rangaraj, K. Kokini, Estimating the fracture resistance of functionally graded thermal barrier coatings from thermal shock tests, Surf. Coating. Technol. 173 (2003) 201–212.
[30] K. Bobzin, N. Bagcivan, T. Brögelmann, B. Yildirim, Microstructure behaviour and influence on thermally grown oxide formation of double-ceramic-layer EB-PVD thermal barrier coatings annealed at 1300 °C under ambient isothermal conditions, Mater. Werkst. 45 (2014) 879–893.
[31] R. Ghasemi, R. Shoja-Razavi, R. Mozafarinia, H. Jamali, M. Hajizadeh-Oghaz, R. Ahmadi-Pidani, The influence of laser treatment on hot corrosion behavior of plasma-sprayed nanostructured yttria stabilized zirconia thermal barrier coatings, J. Eur. Ceram. Soc. 34 (2014) 2013–2021.
[32] B. Liang, C.X. Ding, Thermal shock resistances of nanostructured and conventional zirconia coatings deposited by atmospheric plasma spraying, Surf. Coating. Technol. 197 (2005) 185–192.
[33] E. Altuncu, E.İ. Karaali, G. Erdogan, U. Fatih, A. Turk, The effect of samples geometry and thermal cycling test type on the thermal shock behaviour of plasma sprayed TBCs, Plasma Process. Polym. 6 (2010) 711–715.
[34] H. Jamali, R. Mozafarinia, R. Shoja-Razavi, R. Ahmadi-Pidani, Investigation of thermal shock behavior of plasma-sprayed NiCoCrAlY/YSZ thermal barrier coatings, Adv. Mater. Res. 472–475 (2012) 246–250.
[35] C.G. Zhou, N. Wang, H.B. Xu, Comparison of thermal cycling behavior of plasma-sprayed nanostructured and traditional thermal barrier coatings, Mater. Sci. Eng., A 452–453 (2007) 569–574.
[36] X.C. Zhang, B.S. Xu, H.D. Wang, Y.X. Wu, Y. Jiang, Residual stress distributions within high-temperature coatings, Surf. Coating. Technol. 201 (2007) 6659–6662.
[37] K. Kokini, S.V. Rangaraj, Time-dependent behavior and fracture of functionally graded thermal barrier coatings under thermal shock, Mater. Sci. Forum 492 (2005) 379–384.
[38] A.C. Karaoglanli, A. Turk, I. Ozdemir, F. Ustel, Comparison of oxidation and thermal shock performance of thermal barrier coatings, Mater. Manuf. Process. 30 (2015) 1–7.
[39] A. Moridi, M. Azadi, G.H. Farrahi, Thermo-mechanical stress analysis of thermal barrier coating system considering thickness and roughness effects, Surf. Coating. Technol. 243 (2014) 91–99.
[40] M. Karger, R. Vaßen, D. Stöver, Atmospheric plasma sprayed thermal barrier coatings with high segmentation crack densities: spraying process, microstructure and thermal cycling behavior, Surf. Coating. Technol. 206 (2011) 16–23.
[41] H.Y. Liu, Y.G. Wei, L.H. Liang, Y.B. Wang, J.R. Song, H. Long, Y.W. Liu, Microstructure observation and nanoindentation size effect characterization for micron-/nano-grain TBCs, Coatings 10 (2020) 345.
[42] K. Torkashvand, E. Poursaeidi, M. Mohammadi, Effect of TGO thickness on the thermal barrier coatings life under thermal shock and thermal cycle loading, Ceram. Int. 44 (2018) 9283–9293.

[43] M. Abbas, H.B. Guo, M.R. Shahid, Comparative study on effect of oxide thickness on stress distribution of traditional and nanostructured zirconia coating systems, Ceram. Int. 39 (2013) 475–481.

[44] Z. Chen, H.M. Huang, K. Zhao, W.B. Jia, L. Fang, Influence of inhomogeneous thermally grown oxide thickness on residual stress distribution in thermal barrier coating system, Ceram. Int. 44 (2018) 16937–16946.

[45] X.X. Ren, P. Jiang, X.L. Fan, T.J. Wang, Effect of ceramic layer thickness ratio on thermal shock resistance of La2Ce2O7/YSZ thermal barrier coatings, Rare Met. Mater. Eng. 47 (2018) 3703–3709.